Advanced Steel Construction – Vol. 18 No. 2 (2022) 592–603
DOI:10.18057/IJASC.2022.18.2.8

FULL-FIELD GEOMETRIC IMPERFECTION MEASUREMENT USING A PROJECTION SPECKLE CORRELATION METHOD AND COMPUTATIONAL MODELING OF COLD-FORMED STEEL RACK UPRIGHTS

Jing Shi [1], Ling-Feng Yin [1, 2, *], Xin-Xing Shao [1], Xiao-Yuan He [1], Guan Quan [3] and Zhan-Jie Li [4]

[1] *School of civil engineering, Southeast University, Nanjing 211189, China*
[2] *School of engineering, Tibet University, Lhasa 850011, China*
[3] *School of Civil Engineering and Surveying, University of Portsmouth, Portsmouth PO1 3AH, UK*
[4] *Department of Engineering, SUNY Polytechnic Institute, Utica, NY, USA*
** (Corresponding author: E-mail: eking@seu.edu.cn)*

ABSTRACT

The objective of this study is to provide an innovative and efficient method to measure the geometric imperfections of complex sections such as steel rack uprights and to numerically study their behavior with imperfection sensitivity. Steel rack uprights are generally thin-walled cold-formed steel members, and their compressive capacity and stability are sensitive to initial geometric imperfections. Due to the complexity of the section, accurately measuring the imperfection of such sections could be challenging and labor-intensive. In this paper, the projection speckle correlation method and close-range photogrammetry technique are used to measure the full circumference morphology of the steel rack upright and obtain a 3D point cloud morphology of the member specimen. The initial geometric imperfection is then calculated from the point cloud database. Some characteristics of the imperfection field in the member are further analyzed. The proposed measurement method in this paper, as the first of its kind in the application of geometric imperfection measurement for cold-formed steel structures, has the advantages of low cost, high-speed, and high precision in 3D full-field geometric imperfections for complex sections, and can help further develop more reliable imperfection models for simulations. Moreover, the shell finite element (FE) model is established from the point cloud database along with the ideal member of the upright. Geometric imperfections are also incorporated into the ideal model of the upright in the FE nonlinear collapse analysis to study imperfection sensitivity and compare with the point-cloud model. The results highlight the sensitivity in selecting the imperfection mode shape and its magnitude using the traditional modal approach, which warrants more imperfection databases for the upright.

ARTICLE HISTORY

Received: 15 January 2022
Revised: 9 May 2022
Accepted: 10 May 2022

KEYWORDS

Steel rack uprights;
Initial geometric imperfection;
Projection speckle correlation method;
Finite element simulation

1. Introduction

The rapid development of logistics and e-commerce industries has led to high demand for warehouses filled with steel storage racks from low-rise to high-rise. The main load-bearing components of racks are the uprights, pallet beams, and their connections. Complex racks might have bracings to enhance their seismic performance. Nonetheless, as the main member of the rack's load path, the upright demands a higher safety requirement.

Meanwhile, the members of steel storage racks are usually cold-formed from steel plates (or coils) through rolling or press-braked. In particular, for the upright, it is usually rolled into a complex shape such as Omega sections, with uniaxial symmetry and multiple stiffeners. As a thin-walled steel member, its performance is usually controlled by the stability of various buckling modes (or their interaction) [1]. Consequentially, the strength of the member could be sensitive to the geometric imperfection inherent in the member due to the manufacture, shipping, and storage. For example, the upright member is inevitably subjected to initial geometric imperfection including cross-sectional imperfections and global imperfection caused by torsion or bending due to the press-brake, shipping, and storage [2,3]. The strength of the member is sensitive to these geometric imperfections in terms of both magnitude and shape [4]. Therefore, initial geometric imperfections are required to be considered by current design specifications either implicitly or explicitly depending on approaches [5].

In particular for computational simulation that is commonly used today, how the geometric imperfections are introduced into the model has generated numerous studies [2,6-12]. Meanwhile, significant efforts were also dedicated to investigating the real pattern of imperfections from experimental measurements [13-23] and tried to recommend what the best approach is to include these imperfections in computational modeling. Gao [24] used meter and feeler gauges to measure the initial geometrical imperfections. The linear variable differential transformer displacement transducer (LVDT) [25-27] is a common tool to obtain global geometric imperfection of a steel section along the longitudinal direction. Young [28] added a local imperfection measurement frame with linear ball bearings in addition to the global geometric imperfection measurement frame to simultaneously measure both local and global imperfections of a simple steel section. However, using LVDT to measure geometric imperfections has challenges in keeping it straight with the specimen due to the friction during the translational movement. Meanwhile, the reference points are hard to be locked under the rotation of the specimen during measurement. Large errors can be generated which results in a low accuracy in this type of mechanical topography method. In addition, LVDT measurement can only generate continuous point cloud data in the direction of the measured lines, not global continuous point cloud data over the specimen, which renders the method not able to generate a full-field measurement.

With the technological advances, non-contact methods with high precision are gradually used to obtain a full-field measurement. Zhao [29] combined a 2D laser scanner and a rotating table to construct a three-dimensional imperfection field of cold-formed steel members. Selvaraj and Tran [30,31] used a 3D laser scanner to obtain the initial geometric imperfections of steel sections. Feng [32] used a handheld 3D laser scanner to obtain the 3D geometric imperfections of an I-beam before and after reinforcement and established a digital model based on the 3D point cloud data. Boissonnade [33] placed a regular grid of targets on the web surface and obtained the initial geometrical imperfections through an appropriate numerical treatment of images. These demonstrated the high accuracy and convenience that the 3D laser scanner could bring into measuring geometric imperfections. However, other than the fact that a 3D laser scanner system is usually very expensive, due to the operation nature of the laser beam, the measurement efficiency could be limited when measuring complex sections or large-scale structures.

Another non-contact technique that has great potential is the 3D Digital Image Correlation (3D-DIC), a 3D full-field, non-contact optical technique to measure contour, deformation, and even strain on most materials. It has attracted wide attention and applications in the fields of civil engineering, mechanical engineering, biomedical engineering, and materials science [34-36], due to the benefits of 3D full-field measurement and its high accuracy.

There are applications of DIC in measuring thin-walled members, particularly in composite cylindrical shells that are highly sensitive to imperfections. Kepple et al. [37] used the ATOS system and ultrasonic inspection to measure the geometry and material imperfections of composite cylindrical shells and used the 3D-DIC system to measure their deformation during loading. Degenhardt et al. [38] used a 3D-DIC system (e.g., ARAMIS) to measure the deformation during the test of CFRP cylindrical shells to study the imperfection sensitivity and improve the stochastic modeling of thickness and material imperfections. With the focus of those studies on cylindrical shells with relatively smooth surfaces, the effectiveness of DIC's applications for members with more complex cross-sections and rougher surfaces is worth

further investigation.

In this study, a 3D-DIC with a projector system is proposed using only a two-camera system for high efficiency and used to measure the full-filed geometrical imperfections of a steel rack upright, which has a complex section profile with multiple stiffeners. This, to the best of the authors' knowledge, is the first application of 3D-DIC in geometric imperfection measurement for cold-formed steel structures. The close-range photogrammetry technology is used to establish global coordinates to realize point cloud splicing. The initial geometric imperfection is then calculated by comparing and analyzing the difference between the point cloud data and ideal geometry. The imperfection pattern of the measured 3D full-field imperfection is analyzed and investigated. Based on the measured imperfections, numerical models of the member under axial loading are established. Several strategies of modeling imperfections are investigated against those with the one using the measured full-field imperfection.

2. 3D-DIC Principle

2.1. 3D-DIC method

3D-DIC combines DIC with stereo vision, which enables the measurement of 3D shapes. In our previous work, the parallel IC-GN algorithm was proposed [39] for a multiple-camera system and applied to real-time DIC software. In this study, to reduce the hardware cost, the system is modified to use just two cameras. The mathematical model of the stereo vision with two cameras is shown in Fig.1. The coordinates of point P in the world coordinate system is (X_w, Y_w, Z_w), while in the camera coordinate system is (X_c, Y_c, Z_c) and in the image coordinate system is (u, v), e.g., (u_1, v_1) and (u_2, v_2) for the two image planes shown in Fig.1. The transformation relationship between the image coordinate system and the world coordinate system can be expressed as [40]:

$$\begin{cases} Z_{C1}\begin{bmatrix} u_1 \\ v_1 \\ 1 \end{bmatrix} = M_1 \begin{bmatrix} X_w \\ Y_w \\ Z_w \\ 1 \end{bmatrix} = \begin{bmatrix} m_{11}^1 & m_{12}^1 & m_{13}^1 & m_{13}^1 \\ m_{21}^1 & m_{22}^1 & m_{23}^1 & m_{23}^1 \\ m_{31}^1 & m_{32}^1 & m_{33}^1 & m_{33}^1 \end{bmatrix} \begin{bmatrix} X_w \\ Y_w \\ Z_w \\ 1 \end{bmatrix} \\ Z_{C2}\begin{bmatrix} u_2 \\ v_2 \\ 1 \end{bmatrix} = M_2 \begin{bmatrix} X_w \\ Y_w \\ Z_w \\ 1 \end{bmatrix} = \begin{bmatrix} m_{11}^2 & m_{12}^2 & m_{13}^2 & m_{13}^2 \\ m_{21}^2 & m_{22}^2 & m_{23}^2 & m_{23}^2 \\ m_{31}^2 & m_{32}^2 & m_{33}^2 & m_{33}^2 \end{bmatrix} \begin{bmatrix} X_w \\ Y_w \\ Z_w \\ 1 \end{bmatrix} \end{cases} \quad (1)$$

where M1 and M2 are projection matrices that can be obtained by camera calibration. Four independent equations with three unknown quantities X_w, Y_w, and Z_w can be obtained after eliminating Z_{c1} and Z_{c2}. Then, the world coordinates of the point P can be obtained by solving the overdetermined equation using the least square method. The 3D reconstruction of the object can then be obtained by repeating the process for all the points needed to be calculated.

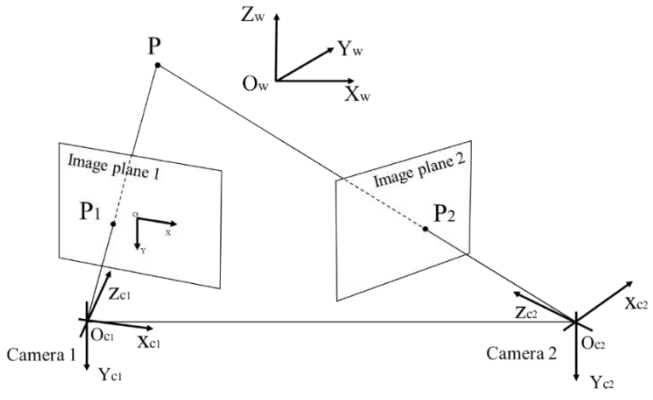

Fig. 1 Stereo vision coordinates with 2 cameras

2.2. Target-based calibration algorithm

The traditional 3D-DIC system cannot be directly used for full-field measurement of complex structures due to the limitation of the field of view. To establish a full-field digital geometric model of the structure, it is necessary to take photos from multiple perspectives. A common approach is to adopt a multi-camera system so point cloud data splicing can be achieved by unifying the extrinsic parameters between the cameras [41,42]. To perform the calibration of these extrinsic parameters between different stereo systems (e.g., O_C), a global coordinate system O_w is required as shown in Fig. 2. H_C (i.e., H_{C1} and H_{C2} in Fig. 2) is the rigid body transformation matrix from the global coordinate system to the camera coordinate system, and H_L (i.e., H_{L1} in Fig.2) is the extrinsic parameter matrix between cameras. A multi-camera system can realize the full-field high-precision measurement of the test specimen, and ensure the consistency of measurement in the time domain as well. As a result, it is suitable for tracking dynamic deformation. However, the cost of hardware and space for setting up cameras will increase. Additional calibration among multiple cameras will also bring additional operational complexity. Genovese [43] used a single SLR camera which was moved to multiple positions around the specimen through a turntable to simulate the effect of multiple cameras. The extrinsic parameters of the camera were calibrated through a control point fixed to the bottom of the specimen. However, this method of placing a control point at one end of the specimen will reduce the spatial resolution when measuring long specimens to ensure sufficient control points in each frame.

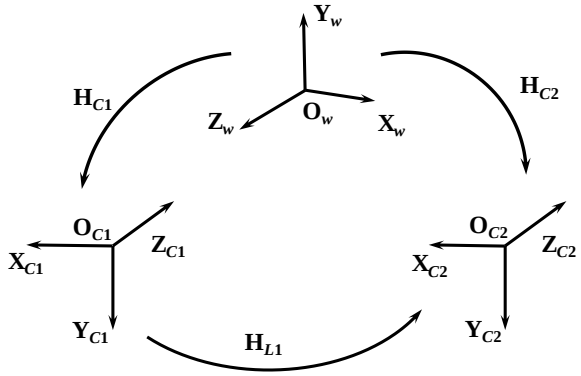

Fig. 2 Rotation and translation transformation of the coordinate system

In this study, the coded points were distributed on the surface of the specimen, and the close-range photogrammetry method develop in our previous work [44] was adopted to carry out 3D reconstruction of the coded points attached to the surface of the specimen, to establish the global coordinate system. There are three main steps of close-range photogrammetry including coded point detection, coded point pre-orientation, and bundle adjustment optimization. First, coded point detection is to obtain the coding and location information of coded points through image preprocessing, edge detection, target screening, and coded point decoding. Second, coded point pre-orientation can obtain the relative orientation between two photos as well as the positions of the cameras in the global coordinate system, which is then used to calculate the cameras' intrinsic and extrinsic parameters between different views. Third, bundle adjustment optimization is a final nonlinear optimization process to reconstruct the global coordinates of the coded points as well as the camera intrinsic and extrinsic parameters [44,45].

The reconstructed coded points have a unified coordinate system, which will move with the movement of the tested part. This unified coordinate system is used as the global coordinate system of the measurement system. For a fixed 3D-DIC system, each movement of the specimen is equivalent to a virtual multi-camera system, and the transformation relationship between the local coordinate system and the global coordinate system can be solved by using the coded points captured from this pose. This method not only achieves the full-field topography measurement of the specimen, but also reduces the number of cameras, calibration times, and operation difficulty. As shown in Fig.3, adjacent cameras represent a 3D-DIC system. Minimization of the following objective function is needed to obtain HCi from the local to global coordinates:

$$E = \sum_{i=1}^{n} \|\boldsymbol{q}_i - (R_i \boldsymbol{p}_i + \boldsymbol{t}_i)\|^2 \quad (2)$$

Where, $H_{Ci} = \begin{bmatrix} R_i & \boldsymbol{t}_i \\ 0 & 1 \end{bmatrix}$, $\mathbf{q}_i$ and $\mathbf{p}_i$ are the coordinates of coded points in global and local coordinate systems, respectively, and R_i and $\mathbf{t}_i$ are the rotation matrix and translation vector from local to global coordinates, respectively.

Through the above function, R_i and $\mathbf{t}_i$ can be obtained through Singular Value Decomposition (SVD) [46].

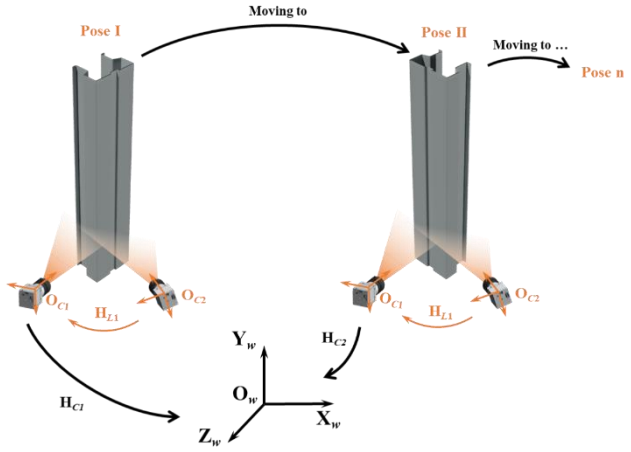

Fig. 3 Virtual multi-camera system setup scheme (for clarity of representation, only two positions of the 3D-DIC systems are illustrated)

The method proposed here can achieve a fast yet accurate solution of the specimen's geometry using just two cameras. Compared to the multi-camera system, the hardware cost is significantly less and also reduces the calibration time, which makes this suitable for a large scale of scanning tasks.

3. System design and precision evaluation

3.1. System design

The 3D-DIC system used in this study consists of two industrial cameras (i.e., IDS UI-3370CP, 2048×2048 Pixel CMOS sensor) and a projector (DLP Light Crafter 4500 Evaluation Module) as shown in Fig.4a. The projector projects speckle images required by the digital correlation calculation, and two industrial cameras form a stereo vision system for the 3D-DIC reconstruction. Coded points were coded by 15-bit concentric circles [47]. A single DSLR camera (NIKON D7100, 6000×4000 Pixel CMOS sensor) was used for close-range photogrammetry to reconstruct the three-dimensional spatial coordinates of the coded points [45]. Industrial cameras have c-port 50mm prime lens (KowA-LM50XC, 50mm, 4/3") and DSLR camera utilizes a Nikon 50mm prime len (50mm F / 1.4g). The object distance of the 3D-DIC system was about 1m, the field of view was about 160×160mm, and the stereoscopic perspective was 35o. In this study, in-house softwares developed by the team as shown in Fig.4b were used for 3D-DIC calculation and the reconstruction of coded points.

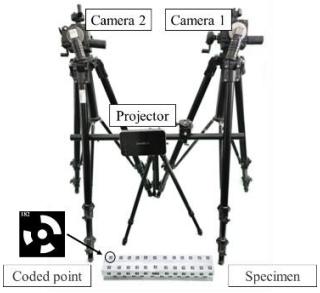

(a) 3D-DIC with projector system

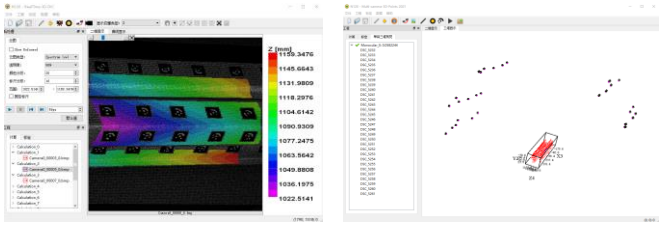

3D-DIC software 3D-points reconstruction software

(b) Measurement softwares

Fig. 4 3D-DIC with projector system

3.2. Precision evaluation of a cylindrical tube

The accuracy of 3D-DIC's measurement relies heavily on not only the accuracy of equipment but also the reconstruction algorithm. In this section, the accuracy of the method applied to imperfection measurement is verified using a simple cylindrical member first before applying to more complex members. First, the 3D-DIC system itself can be accurate to ±0.0016mm. Second, the accuracy of point cloud splicing will be further affected by the identification accuracy of coded points. Combinedly, these determine the accuracy of the measurement, e.g., geometric imperfections in this study.

A verification measurement was conducted using a cylindrical tube with a diameter of 106mm and a length of 280 mm. Coded points were arranged on the outer surface of the tube as shown in Fig. 5a. The specimen with coded points was imaged by a DSLR camera from multiple angles, and the close-range photogrammetry technique was then used to reconstruct the spatial coordinates of the coded points and establish the global coordinate system as illustrated in Fig. 5b. Sequentially, the geometrical morphology point clouds were obtained by moving the specimen, and each local point cloud can cover about 20% of the circumference of the specimen. The stereo vision principle was applied to calculate the coordinate data of coded points in the local coordinate system and the full-filed point cloud of the specimen was spliced. The radius of each point cloud point was converted into cylindrical coordinates. The full-filed point cloud in terms of the radius R is shown in Fig. 5(c), where the blank areas correspond to the coded points. Overall, compared to the perfect geometry, the standard deviation of the calculated radius R is 0.0739. In the region where splicing occurs as shown in Fig. 6, the rectangular region x, the two sets of measurement from point clouds 1 and 2 (i.e., before and after rotating the specimen) are very close. Therefore, the global accuracy of the method used in this study is about ±0.1mm (5% of the thickness), which meets the accuracy requirement.

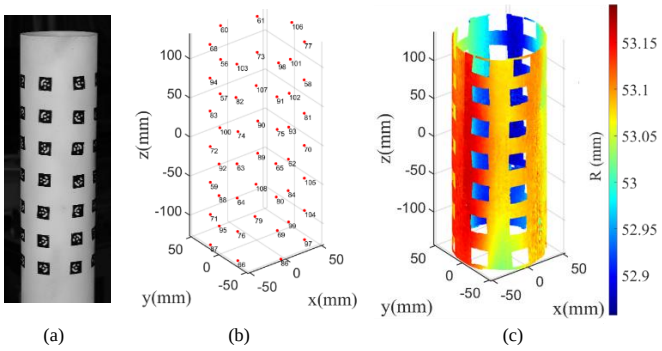

(a) (b) (c)

Fig. 5 Precision analysis test and visualization: a) the cylindrical tube with coded points b) global coordinate of coded points c) measured R results

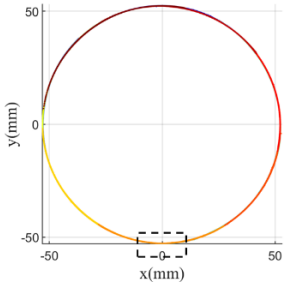

(a) the cross-section with stitching area in rectangle

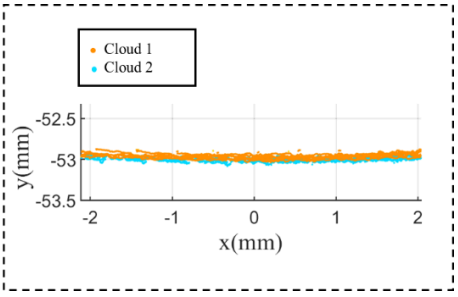

(b) measured point cloud R

Fig. 6 Point cloud stitching (vertical view): a) the cross-section with stitching area in rectangle, b) measured point cloud R in splicing region

4. Geometrical morphology measurement of a rack upright

4.1. Specimen and measurement procedure

As validated before, the accuracy of the developed 3D-DIC system in geometric imperfection is well in the acceptable range. Hence, it was applied to measure the imperfection of a more complex section: a steel storage rack upright. As shown in F, there are several returns and stiffeners within the section. The dimension of the section is a Ω120×85×2.0mm formed by press-braking a Q235B (i.e., yielding stress fy = 235MPa) steel plate. The specimen is 600mm in length, with no perforations. Note that there are obvious localized geometric imperfections at both ends in the specimen due to cutting.

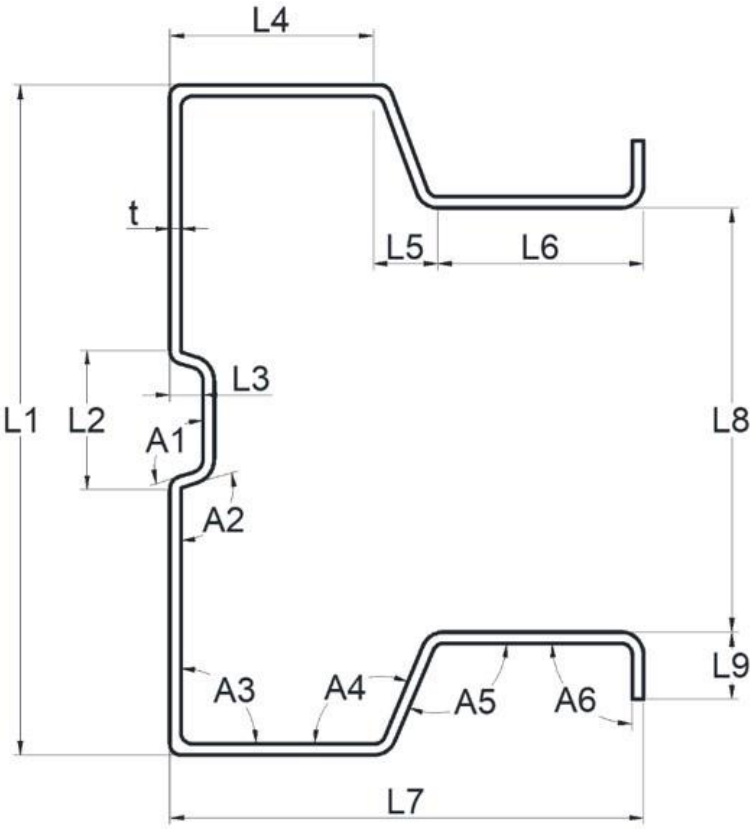

parameter	Design dimension
L1	120.00 mm
L2	25.03 mm
L3	6.00 mm
L4	36.51 mm
L5	11.59 mm
L6	36.90 mm
L7	85.00 mm
L8	76.00 mm
L9	12.00 mm
t	2.00 mm
A1	107°
A2	107°
A3	90°
A4	110°
A5	110°
A6	90°

(a) Design section of the steel rack upright (mm)

(b) Tested specimen

Fig. 7 Steel rack upright: (a) Design section of the steel rack upright (mm) (b) Tested specimen

With multiple turns, the surface of this section could not be measured just by a single pose of cameras due to the obstruction of views and also the camera's limitation of the field of view. Therefore, to measure the specimen, multiple poses were used to ensure the integrity of the morphology measurement result. As illustrated in Fig.8, the annular morphology could be obtained by rotating the specimen 4 times while keeping the 3D-DIC system with the projector fixed. Then the specimen was moved to the new test zone translationally along the longitudinal direction and the next annular morphology is conducted. Particularly, to ensure that there was no untested area, each new test zone needed to have a small amount of overlap with the last zone. Given the length of the specimen was 600mm and the field of view was 160×160mm, 4 translations were needed, which resulted in 16 groups of images. Hence, 16 local morphologies of the specimen in local coordinate systems were obtained by 3D-DIC calculation as illustrated in Fig.8b. In addition, as shown in Fig.8c, the global coordinate system reconstructed from the close-range photogrammetry with the coded points in the local coordinate system was used to obtain the rigid body transformation matrix Hi. With the rigid body transformation matrices, the point clouds could then be unified into the global coordinate system to realize the full-field morphology reconstruction of the specimen as shown in Fig.9.

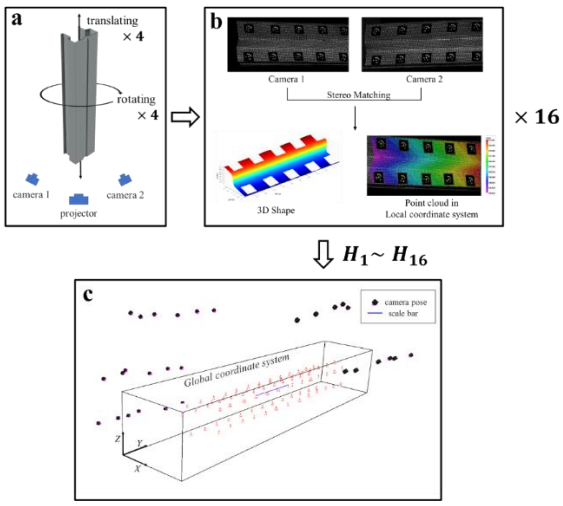

Fig. 8 Measurement procedure

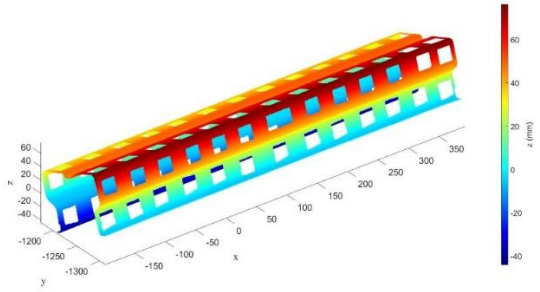

Fig. 9 3D reconstruction result (mm)

4.2. Initial geometric imperfection of the upright

To obtain the geometric imperfection of the specimen, the measured cloud data (580mm cloud data in middle was used for IGI calculation and modeling) is needed to compare with the design value of the member (i.e., idealized perfect geometry). To remove outlier points and reduce the impact of splicing joints, the obtained point cloud will be filtered and smooth first. The iterative closest point algorithm (ICP) [48] was used to register the point cloud data with the idealized geometric point cloud. The following objective function is used:

$$E(R,t)=\frac{1}{n}\sum_{i=1}^{n}\|\boldsymbol{q}_i-(R\boldsymbol{p}_i+\boldsymbol{t})\|^2 \quad (3)$$

where, **q**i and **p**i are coordinates of the idealized geometric point and measured cloud data, respectively, and R and **t** are the rotation matrix and translation vector from the measured cloud data to the idealized geometric point, respectively.

The registered point cloud is the one with a minimum difference from the idealized geometric point cloud. The difference between the two clouds after registration is the geometric imperfection of the specimen. When registering the cloud points using ICP, there are 329 points for each section and a total of 580 sections along the member length. The ICP registration results of the two-cloud data are shown in Fig.10.

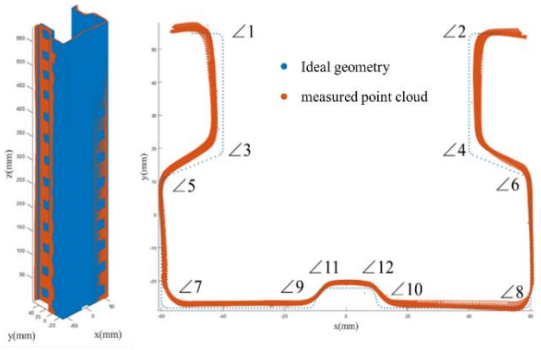

Fig. 10 ICP registration results

As shown in Fig., there are 12 turn angles in this so-called Ω cross-section. These turn angles were calculated along the specimen's length by taking the point cloud data of every 10mm in the z-direction. Then a linear fitting was performed for point clouds on both sides of each turn angle and the angle between the two fitting lines is the turn angle value.

The statistical results of these turn angles are summarized in Table 1 and plotted in Fig. These turn angles possess a difference from 3.92 degrees to 14.02 degrees compared to their design values. Overall, the difference from the design values is relatively large. The differences of turn angles 7 and 8 are comparably small (e.g., below 4%). It is interesting to notice that all the turn angles designed to be 90o are smaller in reality (i.e., see turn angles 1, 2, 7, and 8 in Fig. 11a). This might be from the fact that during manufacture, the pre-brake process tends to overbend the right angle to compensate for potential spring back. Also, the differences of these four turn angles are on the smaller side. For the turn angles 3, 4, 5, and 6 in the flanges, the measured values are all bigger than the design values. Their average differences are bigger than those of 7 and 8 but the majority is still smaller than 10%. On the other hand, turn angles in the web (i.e., 9-12) demonstrate a much bigger difference from their design angle. The difference is around 25% for all these four angles. These four angles are intended to form the stiffener in the web and the large difference of these turn angles might result from the difficulty in precision control during the press-brake within such a small length. Furthermore, Figb illustrates the variation of these turn angles along the specimen's length in the z-direction. Again, turn angles 7 and 8 show less fluctuation along the length. All others show a much larger fluctuation.

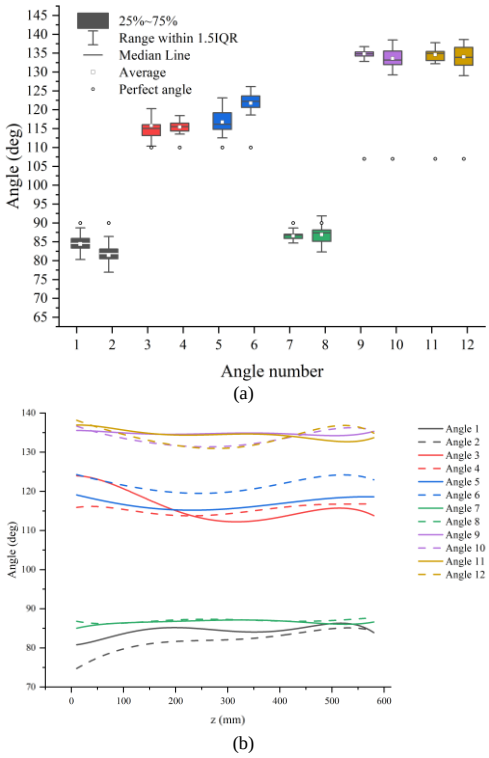

Fig. 11 Turn angles: (a) Statistics of turn angles (b) fluctuation of turn angles along the z-direction

Table 1
Turn angle results from measurement

Number	Measured results	Design value (deg)	error
1	84.40	90	-6.22%
2	82.21	90	-8.66%
3	115.79	110	5.26%
4	115.34	110	4.85%
5	116.75	110	6.14%
6	121.70	110	10.64%
7	86.60	90	-3.78%
8	86.88	90	-3.47%
9	134.76	107	25.94%
10	133.42	107	24.69%
11	134.43	107	25.64%
12	133.64	107	24.90%

The difference changes the overall geometry of the specimen. Turn angles 9, 10, 11, and 12 in the web are all larger than the design value by 25 degrees, which made the stiffener wider and more curved than the design. The width of the stiffener is 34.70mm which is 38.8% more than the design width of 25.03mm, and the depth of the stiffener is 6.64mm with an increase of 10.6% compared with the design depth of 6.0 mm. The difference of turn angles 5 and 6 in the middle of the flanges makes the flanges deviate from the designed position, which renders the section a distortional imperfection mode. This is further illustrated in Fig, where the measured section versus the design section is shown along the length. While the web is relatively flat, the flanges are distorted to the outside. In buckling, this corresponds to the outward distortional buckling mode. The distortion amplitude along the z-direction is large at both ends and small in the middle.

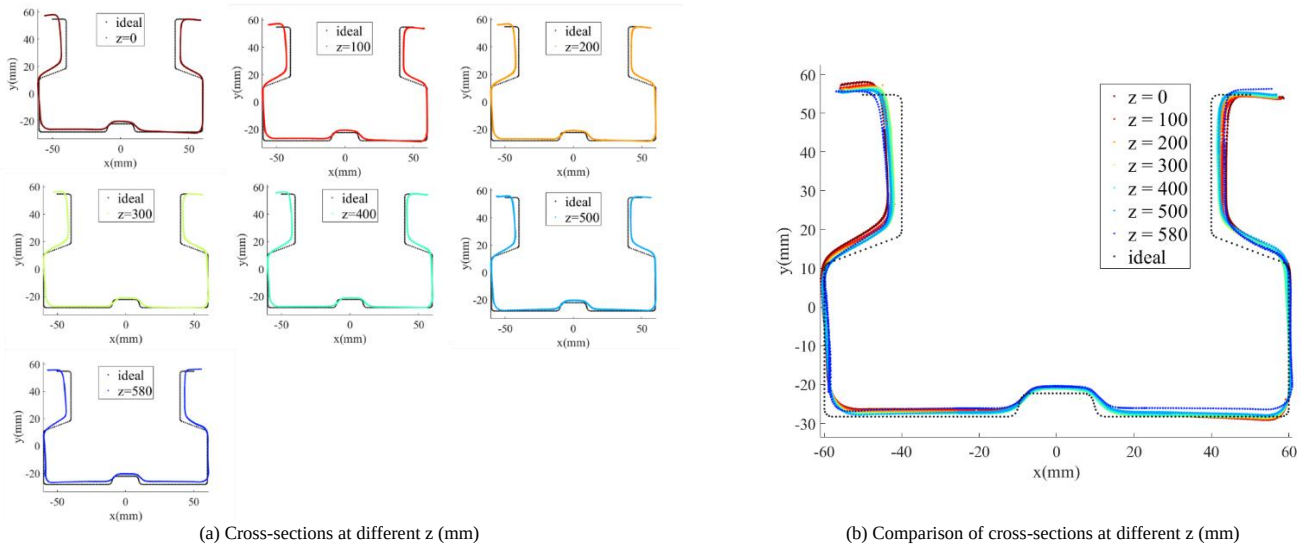

(a) Cross-sections at different z (mm) (b) Comparison of cross-sections at different z (mm)

Fig. 12 Cross-sectional view of the specimen: (a) Cross-sections at different z (mm) (b) Comparison of cross-sections at different z (mm)

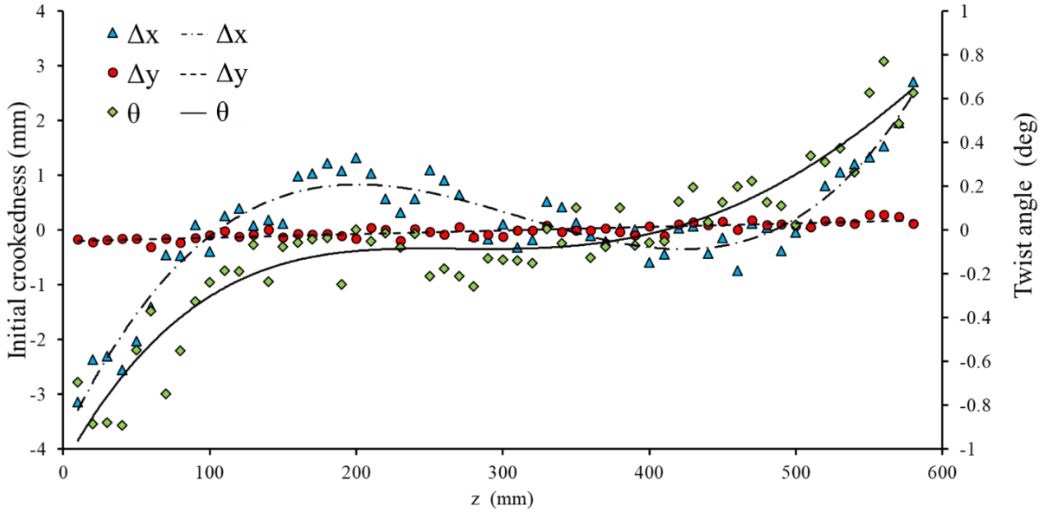

Fig. 13 Initial crookedness and relative twist

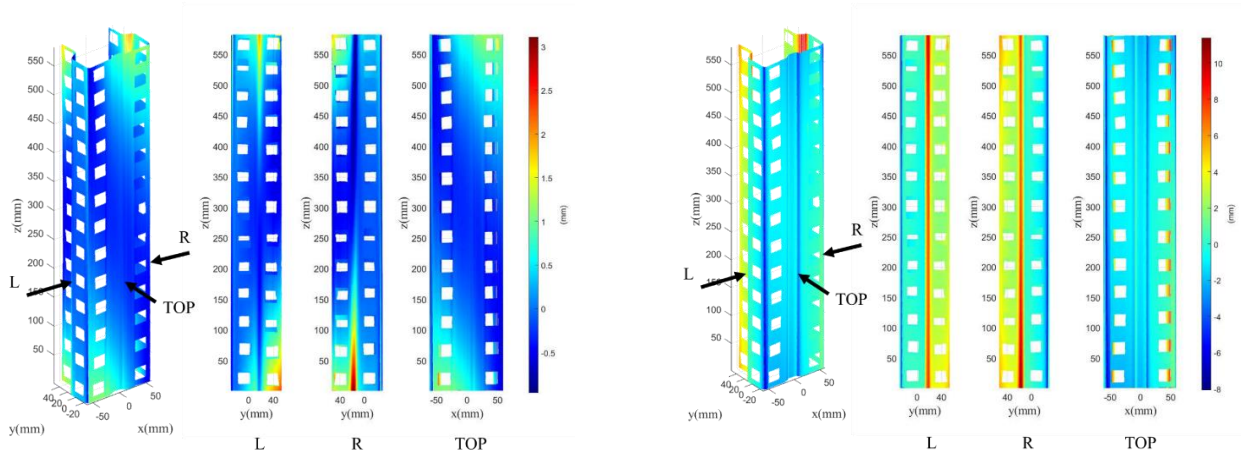

(a) Smoothness (b) Contour error

Fig. 14 Full-field geometric imperfections: (a) Smoothness (b) Contour error

5. Numerical analyses

Thin-walled members are subjected to complex instabilities, and geometric imperfections have been shown to have a significant impact on their ultimate strength and post-buckling mechanisms. Hence, in computational modeling, careful treatment of geometric imperfection is needed, which demands the specification of both the imperfection distribution and magnitude. Two approaches are generally adopted to simulate the imperfection field: 1) using measured imperfection field; 2) a modal approach using buckling mode shape(s) with a certain magnitude. With the full-field imperfection measured from above for this rack upright section, the geometric imperfection can be incorporated directly from the measured cloud data. Meanwhile, the traditional modal approach is also used here to highlight the effectiveness of this approach in strength prediction against that from the full-field measurement.

5.1. Computational model details

Shell finite element (FE) modeling using the commercial finite element package ABAQUS [49] is established with those geometric imperfections. However, ultimate strength prediction and investigation of collapse behavior necessitate the inclusion of material nonlinearity as well. The solutions of these models can also be influenced by several other model inputs, such as residual

stresses, plastic strain, yield criteria, material model, boundary conditions, and also the fundamental mechanics, particularly concerning element selection and solution schemes [6].

In this study, residual stresses and initial plastic strains are not included. Material is the Q235 steel with a with Young's modulus E = 206,000 MPa, Poisson's ratio v = 0.28, and yield stress of 235 MPa. Material is modeled as homogeneous and isotropic with von Mises yield criteria with the plasticity shown in Table 2. The finite element models are shown in Fig.15. The perfect (or ideal) model and point cloud model are respectively established by using the design values and point cloud data (note, interpolation is used to complete the blank space due to coded points.).

Table 2
Material plasticity in ABAQUS model

Yield Stress (N / mm2)	Plastic Strain
235	0
248	0.00124
294.5	0.03936
332.48	0.07749
361.975	0.115621
393.042	0.1537
395.682	0.19187
399.896	0.23

In the model, shell element S4R in the ABAQUS library is selected to model the member and solid element C3D8R is selected to model the loading plates. A fine mesh is chosen for both the perfect and point cloud models. The mesh size for the perfect model is 5 mm and the point cloud model is 2mm to account for the potential large un-smoothness in the member. It is worth noting that for both models, a convergence analysis was shown that the mesh had a negligible impact on the solution with a fine mesh like this. The mesh size for loading plates is 10mm. A shell-solid coupling constraint is applied between the upright and the loading plates, the fixed constraint (U1=U2=U3=UR1=UR2=UR3=0) is applied to the bottom loading plate, while the fixed constraint (except U3≠0 in the axial direction) is applied to the top-loading plate. Finally, a 5mm displacement load was applied in the axis direction to simulate a column member. The solution scheme for the collapse analysis is the arc-length method (the modified Riks method [49] in ABAQUS).

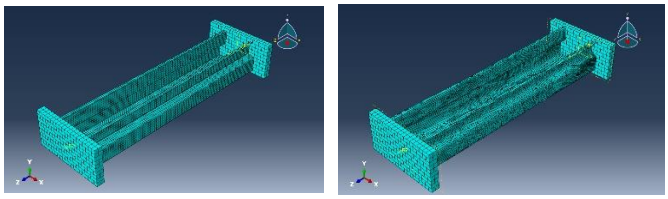

(a) Ideal Model (b) Point cloud model

Fig. 15 Numerical models: (a) Ideal model (b) Point cloud model

5.2 Geometric imperfections

First, for the ideal model, an eigenvalue analysis was conducted. A selective set of modes was pulled out and shown in Fig.16. For thin-walled members, mode categorization can be challenging due to the complex buckling natures and their potential interaction. A laborious visual inspection of the modes can determine the mode type as listed in Fig.16. For the traditional modal approach of modeling geometric imperfections, these will be the fundamental shapes assumed in the model. For a short member like this, the dominated modes are the distortional modes. The 4th to 7th modes shown also demonstrate interaction among distortional modes (or with local modes). Only the 22nd mode visually demonstrates a strong local buckling trait. The numerical models herein incorporate the selected modes and their combinations with varying magnitude. Global imperfections such as camber, bow, and twist recommended in [3] are not included. Much higher modes need to be extracted to potentially identify those modes. Also, based on the full-fielded measurement in Fig, the bow effect is negligible. There is initial crookedness in the x-direction but the shape is significantly different from the camber assumed in [3] – a half-sine wavelength. Similarly, for the twist mode, in the measured specimen, it largely resides towards the ends unlike the one assumed in [3].

For the traditional modal approach, magnitude needs to specify for the mode shapes being incorporated in the model. In this study, several magnitudes are selected for each mode and their combinations as listed in Table 3. The 25%, 50%, 75%, and 95% percentiles related to the imperfection magnitude are the statistical data on lipped channel sections in [3]. While the upright section is different from the lipped channel, with lack of a more comprehensive statistical data of upright right sections, those numbers in [2] were adopted for the study here to illustrate the impact of magnitude selection. In [3], Type I imperfection mode is treated as the one corresponding to local mode imperfection while Type II is the distortional mode imperfection. Meanwhile, based on the full-field measurement shown in Fig, the measured imperfection demonstrates a strong outward distortional mode. The maximum magnitude of this imperfection mode (corresponding to Type II in [3]) is calculated and plotted in Fig.17. This magnitude is also used to scale the distortional mode imperfections in the model as listed in Table 3. On the other hand, the Type I imperfection (i.e., local mode) is not significant from the measured full-field data, hence no measured magnitude for the local mode imperfection (i.e., the 22nd mode) is scaled in the model. In addition, mixed-mode imperfections (e.g., local and distortional) using the traditional modal approach are also considered in this study as listed in Table 3. Only the mixed modes between local (i.e.,22nd) and distortional (e.g., 1st) are considered here. Note that the magnitude for each mode is based on the value of their individual percentiles in [3]. For distortional mode imperfection, even though from measured data in Fig, the imperfection is observed as outward distortional mode, not inward, the potential positive and negative magnitudes that represent the outward and inward distortional modes, respectively, are considered for some modes as well.

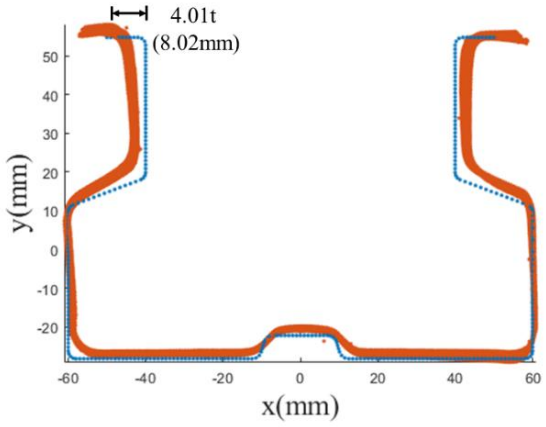

Fig. 17 Maximum measured magnitude of distortional mode imperfection

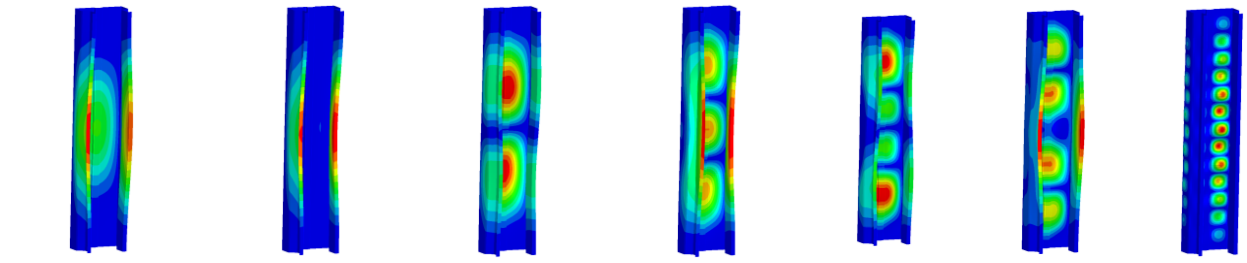

(a) 1st mode: 730kN – outward distortional mode
(b) 2nd mode: 881kN – asymmetrical distortional mode
(c) 3rd mode: 893kN –higher-order distortional mode
(d) 4th mode: 1035kN – interactive distortional mode
(e) 5th mode: 1171kN – interactive distortional mode
(f) 7th mode: 1275kN – interactive distortional mode
(g) 22nd mode: 2010kN – local mode

Fig. 16 eigenmodes of the upright section

Table 3
Imperfection magnitudes

Mode	Mode type	Imperfection magnitude based on percentile				
		25%	50%	75%	95%	Measured magnitude
1	outward D	0.64t	0.94t	1.55t	3.44t	4.01t
2	asymmetrical D	0.64t	0.94t	1.55t	3.44t	4.01t
3	higher-order D	0.64t	0.94t	1.55t	3.44t	4.01t
4	interactive D	0.64t	0.94t	1.55t	3.44t	4.01t
5	interactive D	0.64t	0.94t	1.55t	3.44t	4.01t
7	interactive D	0.64t	0.94t	1.55t	3.44t	4.01t
22	L	0.14t	0.34t	0.66t	1.35t	-
1 & 22	D/L	0.14t*22+0.64t*1	0.34t*22+0.94t*1	0.66t*22+1.55t*1	1.35t*22+3.44t*1	-
1(-) & 22	D/L	0.14t*22-0.64t*1	0.34t*22-0.94t*1	0.66t*22-1.55t*1	1.35t*22-3.44t*1	-

Note: t is the thickness of the member

Table 4
Ultimate loads of all models

	Ultimate load (kN)					Relative difference to the point cloud model (%)				
Ideal	188.4									
Point cloud	176.0									
Mode	Imperfection magnitude based on percentile					Imperfection magnitude based on percentile				
	25%	50%	75%	95%	Measured magnitude	25%	50%	75%	95%	Measured magnitude
1	183.1	180.7	176.1	163.9	160.8	4.0	2.7	0.1	-6.9	-8.7
1(-)	192.3	192.4	182.1	161.0	156.1	9.3	9.3	3.5	-8.5	-11.3
2	188.5	188.4	187.2	177.1	174.5	7.1	7.1	6.4	0.6	-0.9
3	180.5	176.3	168.1	146.3	121.6	2.5	0.1	-4.5	-16.9	-30.9
4	181.7	178.8	173.1	148.8	143.7	3.3	1.6	-1.6	-15.5	-18.4
5	180.9	177.4	169.9	150.0	123.9	2.8	0.8	-3.5	-14.8	-29.6
7	182.2	178.7	171.7	153.9	149.8	3.5	1.5	-2.5	-12.5	-14.9
7(-)	181.3	178.3	173.3	158.7	152.8	3.0	1.3	-1.5	-9.9	-13.2
22	179.1	173.2	164.2	148.4	-	1.7	-1.6	-6.7	-15.7	-
1 & 22	182.3	177.4	167.2	147.4	-	3.6	0.8	-5.0	-16.2	-
1(-) & 22	191.9	190.0	176.3	147.3	-	9.0	8.0	0.2	-16.3	-

5.3 Nonlinear collapse analyses

The load versus displacement (i.e., end-shortening) responses were extracted from the nonlinear collapse analyses of all models with a variety of geometric imperfections based on the traditional modal approach in Table 3. The result of the point-cloud model which represents the measured imperfection was carried out as well, along with the perfect model (or ideal model) without any imperfections. Note that the point-cloud model represents a true dimension of the physical specimen, which should provide the closest prediction of the member's actual behavior. The ultimate loads of each model (i.e., peak load from the load vs. displacement response) are summarized in Table 4.

First, for the point cloud model, the predicted ultimate load is 176.0 kN. This is lower than the perfect model's prediction, 188.4 kN, which represents a 7% difference compared to the point cloud model. The initial stiffness of the two models is close but slightly different. The member is in the inelastic buckling regime (i.e., the critical buckling load is 729.6 kN). Both the models demonstrate large flange deformation in the middle region of the member at the peak, which corresponds to a distortional deformation. However, the ideal model has an outward flange distortional deformation (Fig. 18b) while the point cloud model shows an inward one (Fig.18c). Material nonlinearity further deteriorates the outward and inward distortional deformation, respectively, in the post-peak regime and creates slight localization in the middle (Fig. 18d-e). This is an interesting observation from the point cloud model given that the imperfect model possesses an outward distortional imperfection as measured (Fig. 12). The von mises stress contours of the two models at three selected points along with the load-displacement responses in Fig. 19 further illustrate the differences in the yielding mechanism. The yielding distribution is quite different in the flange lips between the two models, which eventually leads to different collapse mechanisms (i.e., inward or outward distortional). Note that red represents the yielding elements. The lips in the point cloud model have yielding regions in the middle of the member while still in elastic in the perfect model.

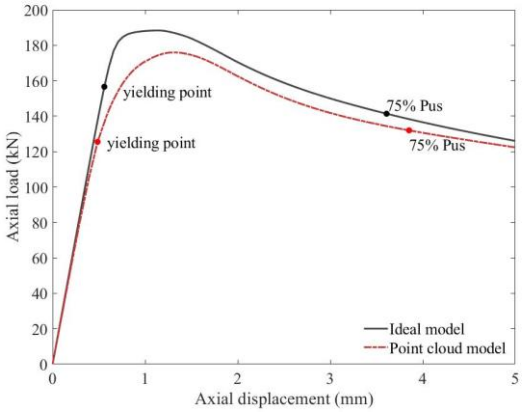

(a) Load-displacement responses

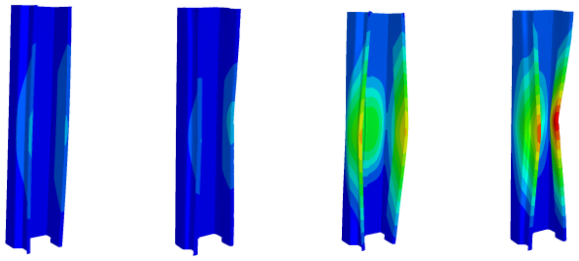

(b) Ideal model: peak | (c) Point cloud model: peak | (d) Ideal model: post-peak (75% of peak load, Pus) | (e) Point cloud model: post-peak (75% of peak load, Pus)

Fig. 18 Load-displacement responses of ideal and point cloud models with deformation modes

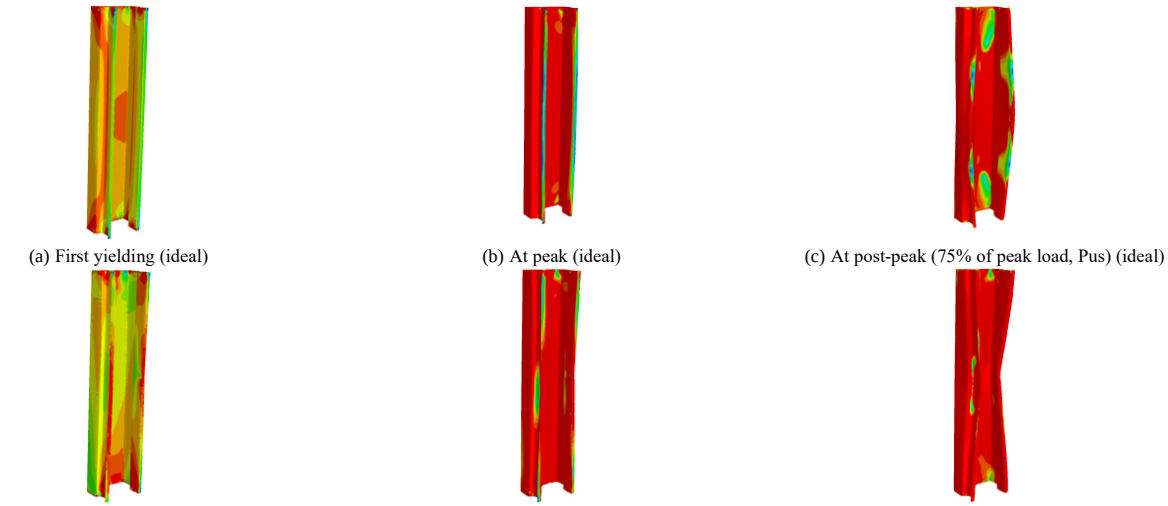

(a) First yielding (ideal) (b) At peak (ideal) (c) At post-peak (75% of peak load, Pus) (ideal)

(d) First yielding (point cloud) (e) At peak (point cloud) (f) At post-peak (75% of peak load, Pus) (point cloud)

Fig. 19 Von Mises stress contours of ideal and point cloud models

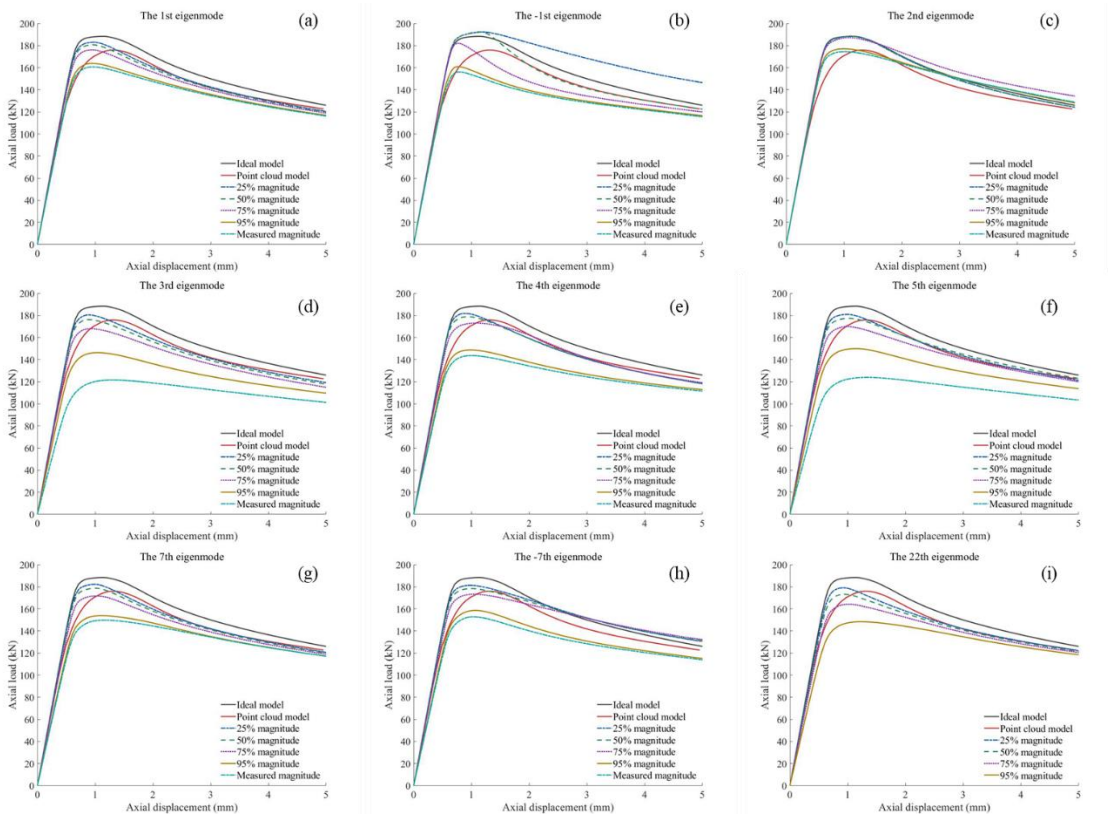

Fig. 20 load-displacement responses with a variety of eigenmodes and magnitudes

Second, the traditional modal approach relies on the buckling mode shapes that are to be assumed as the geometric imperfections of the model. Usually, the 1st buckling mode bears relatively heavyweight in consideration of geometric imperfections, which is usually thought of as a sympathy mode to imperfection-sensitive structures. For this member, the 1st buckling mode is a distortional buckling mode. A positive magnitude scaled based on this mode will provide an outward distortional imperfection, which matches the measured imperfection on the cross-sectional level (Fig. 12). From the results shown in Fig. 20a and Table 4, the impact of the magnitude of the imperfection can be observed. Using 25th and 50th percentiles of imperfection magnitudes still overestimate the peak load by more than 2.7% compared to that of the point cloud model. While using the 95th percentile of magnitude underestimate around 7%. Using the measured magnitude in Fig. 17 predicts an even lower peak load than that of the 95th percentile. The closest prediction in terms of peak load is using the 75th percentile magnitude, which shows a difference less than 0.1% of that of the point cloud model. However, the initiation of the yielding is quite different and the failure mode is different as well. The failure modes and yielding at peak and post-peak of the 75th percentile model are shown in Fig. 21a-d. The failure at peak and post-peak all demonstrate an outward distortional deformation, which is different from those of the point-cloud model. The yielding distribution reveals that the lips in this model are still in elastic from Fig. 21c while the section has yielding regions in the middle length of the member in the point cloud model (Fig. 19e). Meanwhile, if a negative magnitude is scaled using this mode, it represents an inward distortional imperfection. This is different from what is observed from measured imperfection in Fig. 12 but worth investigating the impacts on strength and failure mode. Clearly, based on the strength prediction in Table 3 and Fig. 20b, the assumed imperfection field generate a large error. The closest prediction in strength is also the 75th percentile magnitude but has a 3.5% error compared to that of the point cloud model. However, the failure modes and yielding distribution as illustrated in Fig. 21e-f for the 75th percentile model shows an inward distortional deformation, which is similar to those of the point cloud model.

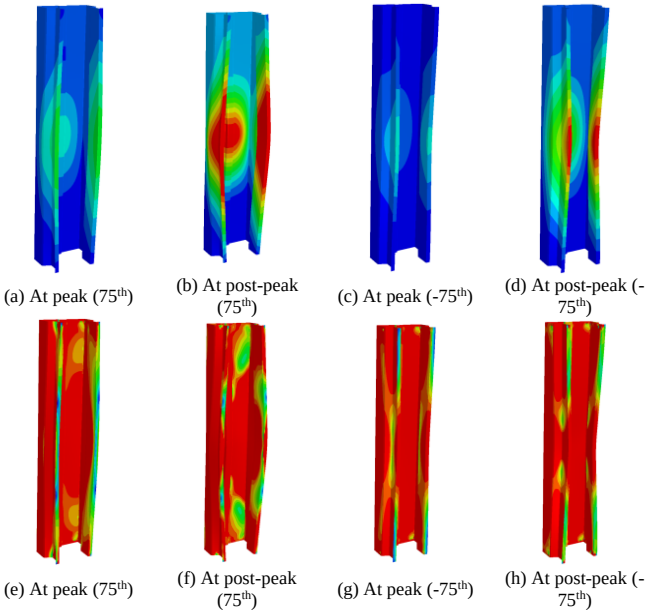

Fig. 21 Failure modes and von Mises stress contour of the model with 1st mode imperfection: (a)-(d) 75th percentile magnitude; (e)-(h) negative 75th percentile magnitude

Third, the 2nd eigenmode is an asymmetrical distortional mode. Using this mode as imperfection with a magnitude close to the 95th percentile and measured magnitude can predict a close strength to that of the point cloud model (both within 1%) as shown in Fig. 20c and Table 4. However, the failure modes and yielding distribution at peak and post-peak showed in Fig. 22 reveal a different failure mechanism compared to those of the point cloud model. The failure mode is heavily influenced by the initial imperfection mode shape.

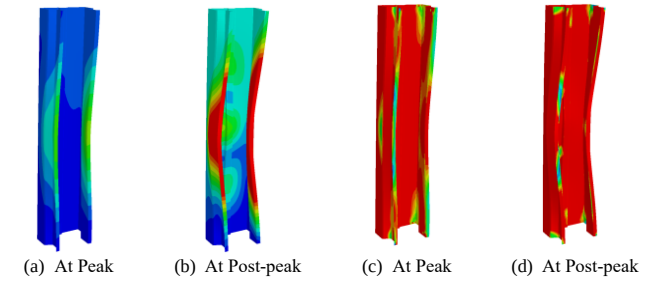

Fig. 22 Failure modes and von Mises stress contour of the model with 2nd mode imperfection – 95th percentile magnitude: (a)-(b) failure modes; (c)-(d) von Mises stress contour

Fourth, the 3rd mode is identified as a distortional mode with two half-waves. The 50th percentile magnitude with this imperfection mode predicts a close strength compared to the point cloud model (i.e., within 0.2% difference from Table 4). Others have relatively large errors, especially using the measured magnitude in Fig. 20d. Large imperfection models also lead to a large difference in the initial stiffness of the member as well compared to that of the point cloud model. Meanwhile, the failure modes and yielding distribution at peak and post-peak are quite different from those of the point-cloud model as shown in Fig. 19.

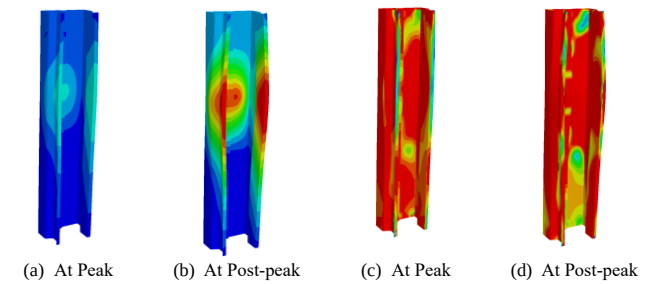

Fig. 23 Failure modes and von Mises stress contour of the model with 3rd mode imperfection – 50th percentile magnitude: (a)-(b) failure modes; (c)-(d) von Mises stress contour

Fifth, modes 4, 5, and 7 are all identified as interactive modes between different orders of distortional modes. Or it might be identified as conventional local and distortional interaction. All these three models predict a relatively small error in strength compared to the point cloud model using the 50th percentile magnitude as shown in Fig. 20e-h. However, using the measured magnitude, the errors are big as shown in Table 4. Also, the initial stiffness of the member using this magnitude has a large difference compared to that of the point cloud model. In Fig. 24, the failure mode of the 4th mode imperfection with 50th percentile magnitude shows an inward distortional deformation similar to that of the point cloud model. All others have an outward distortional deformation similar to the ideal model. In addition, more deformation localization in the web is observed in all these models.

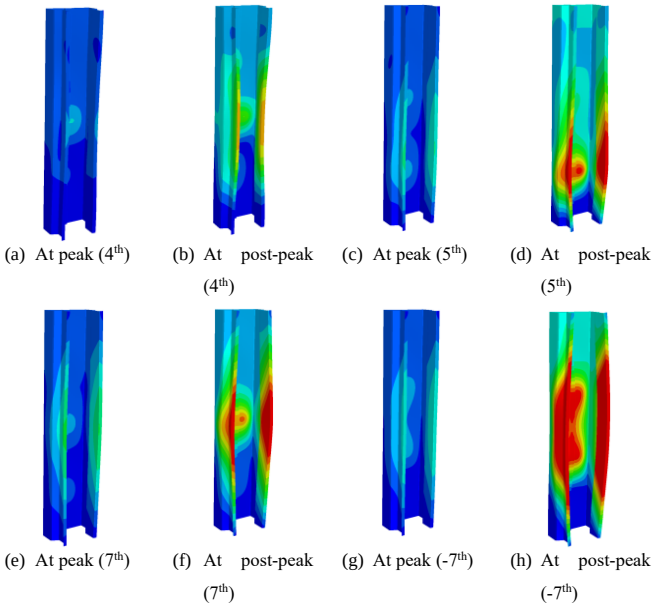

Fig. 24 Failure modes of the models with 4th, 5th, and 7th (positive and negative) mode imperfections – 50th percentile magnitude

Sixth, the 22nd mode is the first mode demonstrating a strong local buckling trait. The models with 25th and 50th percentile magnitudes predict a strength within 2% of the point cloud model as shown in Fig. 20i and Table 4. However, the failure mode and yielding distribution (Fig. 25) are different compared to those of the point cloud model as shown in Fig. 23. More deformation localization in the web is observed in these models.

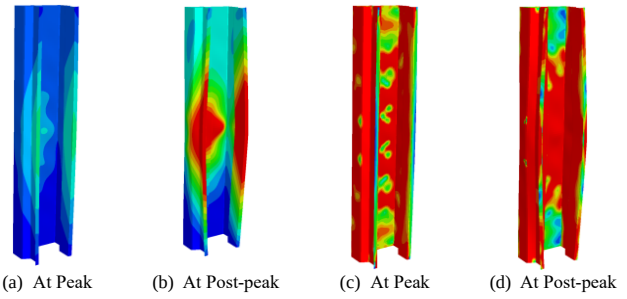

Fig. 25 Failure modes and von Mises stress contour of the model with 22nd mode imperfection – 50th percentile magnitude: (a)-(b) failure modes; (c)-(d) von Mises stress contour

Finally, a combination of 1st mode (i.e., distortional) and 22nd mode (i.e., local) with varying magnitude are investigated. The 1st mode is scaled with both positive and negative magnitudes. The load-displacement responses are plotted in Fig. 26 and their strengths are summarized in Table 4. With a positive magnitude of the 1st mode (i.e., outward imperfection) with the 22nd mode, a 50th percentile magnitude is able to predict a strength within 1% of the point cloud model; while the negative case (i.e., inward imperfection), a 75th percentile magnitude predicts a strength within 0.5%. The failure modes and yielding distribution of these two models are illustrated in Fig. 27. They reveal the different failure mechanisms compared to that of the point cloud model. With the inward distortional imperfection (Fig. 27e-h), this model demonstrates a similar inward distortional failure but differs in the web region, where more localization can be observed compared to that of the point cloud model.

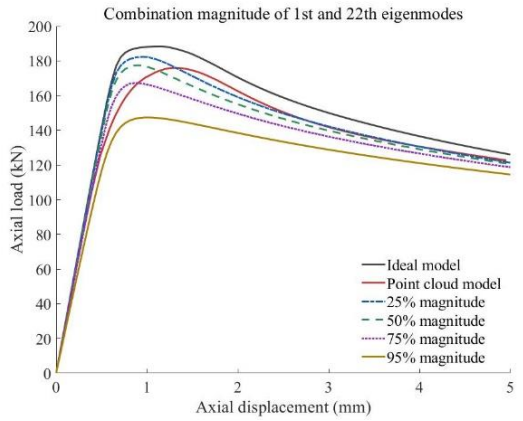

(a) 1st and 22nd combination

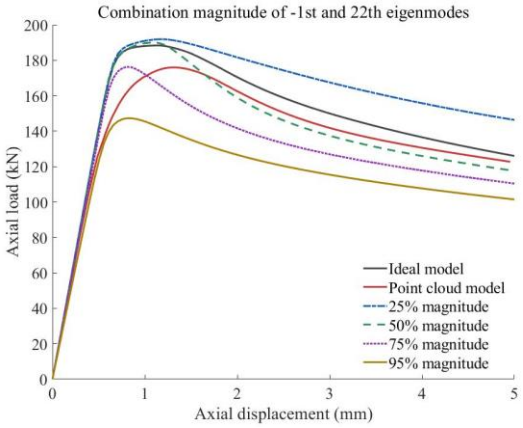

(b) 1st (negative) and 22nd combination

Fig. 26 Load displacement responses of combined mode imperfections

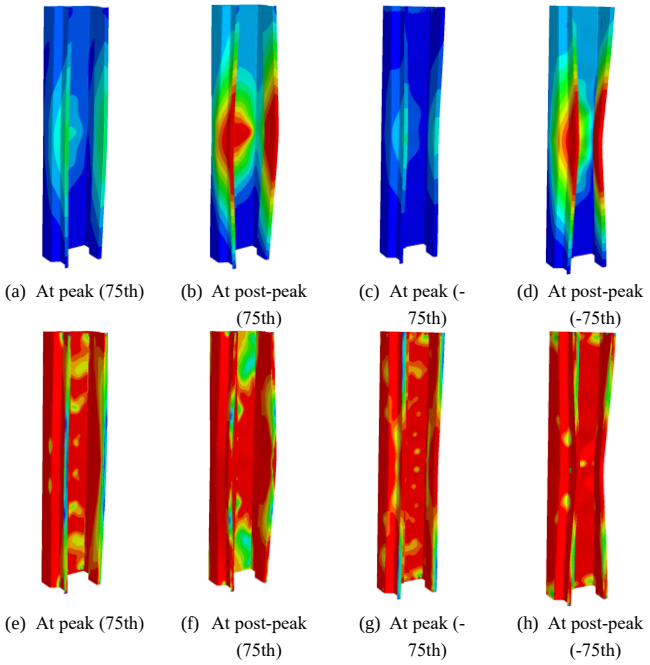

(a) At peak (75th) (b) At post-peak (75th) (c) At peak (-75th) (d) At post-peak (-75th)

(e) At peak (75th) (f) At post-peak (75th) (g) At peak (-75th) (h) At post-peak (-75th)

Fig. 27 Failure modes and von Mises stress contour of the model with 1st and 22nd mode imperfections: (a)-(d) 50th percentile magnitude; (e)-(h) negative 1st mode with 75th percentile magnitude; (a,b,e,f) failure mode; (c,d,g,h) von Mises stress contour

6. Discussions

The proposed method using 3D-DIC is able to construct a full 3D imperfection field for complex section profiles like the one in the rack upright. With the accuracy this method can achieve, details of the characteristics of the imperfections in these members can be further analyzed and studied. Useful information can be collected to aid the future analysis of direct modeling of geometric imperfections. This requires a large data-gathering effort by scanning more sections and forming the needed 3D full-field imperfection database.

Meanwhile, while simulating the member with measured 3D full-field imperfection can be realized, developing new geometric imperfection models based on a large database to simulate the real imperfection field would be more helpful for efficient modeling of the member. In particular, the measured full-field imperfection in this study reveals a potentially different pattern of the upright section compared to the conventional lipped C sections.

Moreover, the numerical simulation using the traditional modal approach highlights the sensitivity of the simulation with the selection of the imperfection mode shape and its magnitude. The consistent and reliable prediction of the load-displacement response with correct failure modes is challenging as shown from this study. While more advanced modal approaches are available (e.g., [3]), the study herein is not able to perform due to the limited dataset obtained in this study so far. With the aforementioned data gathering, future studies in this aspect will be pursued.

7. Conclusions

In this paper, an efficient measurement method using the 3D-DIC system with projection speckles is proposed and applied to measure the initial geometric imperfections of steel rack uprights. This system utilizes the projection speckle correlation method and close-range photogrammetry. As the first of its kind in the application of measuring geometric imperfections of cold-formed steel structures, it is demonstrated to possess high accuracy and efficiency. The application to the complex steel rack upright member establishes a 3D point cloud of the geometry and enables a full-field geometric imperfection for such a complex section with so many stiffeners. Analysis of the full-field imperfection reveals a potentially different imperfection pattern of the upright section compared to the conventional lipped C sections. Numerical modeling from the point cloud model and ideal member models incorporated with different imperfections using the traditional modal approach highlights the need for a careful selection of the imperfection mode shape and its magnitude in simulation. In particular, for the upright section, the proposed measurement method could enable a large set of geometric imperfection data gathering with relatively low cost due to the efficiency of the system. This can assist a large data-gathering effort by scanning more sections and forming the needed 3D full-field imperfection database, thus enabling the development of new geometric imperfection models and aiding the future analysis of direct modeling of geometric imperfections.

Acknowledgments

The authors would like to acknowledge financial support from the Natural Science Foundation of Jiangsu Province (BK20191268) and the Technology Development Fund for Local Regions from Central Government (XZ202201YD0032C). Any opinions, findings, and conclusions, or recommendations expressed in this material are those of the author(s) and do not necessarily reflect the views of the above funding agencies.

References

[1] Zhao X, Dai L, Huang Z, et al. Review of the research on steel storage rack structures[J]. Engineering Mechanics, 2019, 36(08): 1-15.
[2] Schafer B W, Peköz T. Computational modeling of cold-formed steel: characterizing geometric imperfections and residual stresses[J]. Journal of Constructional Steel Research, 1998, 47(3).
[3] Zeinoddini V M, Schafer B W. Simulation of geometric imperfections in cold-formed steel members using spectral representation approach[J]. Thin-Walled Structures, 2012, 60.
[4] Pastor M M, Bonada J, Roure F, et al. Residual stresses and initial imperfections in non-linear analysis[J]. Engineering Structures, 2013, 46.
[5] Specification for Structural Steel Buildings[S]. ANSI/AISC 360-2016.
[6] Schafer B W, Li Z, Moen C, et al. Computational modeling of cold-formed steel[J]. Thin-Walled Structures, 2010, 48(10).
[7] Dinis P B, Camotim D, Silvestre N. FEM-based analysis of the local-plate/distortional mode interaction in cold-formed steel lipped channel columns[J]. Computers and Structures, 2007, 85(19).
[8] Ashraf M, Gardner L, Nethercot D A. Finite element modelling of structural stainless steel cross-sections[J]. Thin-Walled Structures, 2006, 44(10).
[9] Chou S M, Chai G B, Ling L. Finite element technique for design of stub columns[J]. Thin-Walled Structures, 2000, 37(2).
[10] Camotim D, Silvestre N, Dinis P B. Numerical Analysis of Cold-Formed Steel Members[J]. International Journal of Steel Structures, 2005.
[11] Gardner L, Nethercot D A. Numerical Modeling of Stainless Steel Structural

Components—A Consistent Approach[J]. Journal of Structural Engineering, 2004, 130(10).
[12] Cao H P, Hancock G J. Numerical simulation of high strength cold-formed purlins in combined bending and shear[J]. Journal of Constructional Steel Research, 2010, 66(10).
[13] Schafer B W. Cold-formed steel behavior and design: analytical and numerical modeling of element and member with longitudinal stiffeners. Thesis, Ithaca, New York: Cornel University, 1997.
[14] Ingvarsson L. Cold-forming residual stresses and box columns built up by two cold-formed channel sections welded together. Stockholm, Sweden: The Royal Institute of Technology, 1997.
[15] Lau SCW. Distortional buckling of thin-walled columns. PhD thesis, Sydney, Australia: University of Sydney, 1988.
[16] Bernard E S. Flexural behavior of cold-formed profiled steel decking. PhD thesis, Cydney, Australia: University of Sydney, 1993.
[17] Schafer B W, Zeinoddini V. Global imperfections and dimensional variations in cold-formed steel members[J]. International Journal of Structural Stability & Dynamics, 2011.
[18] Peterman K D, Schafer B W. Sheathed Cold-Formed Steel Studs under Axial and Lateral Load[J]. Journal of Structural Engineering, 2014, 140(10).
[19] Kwon Y B, Hancock G J. Tests of cold-formed channels with local and dlstortional buckling[J]. Journal of Structural Engineering New York (N.Y.), 1992, 118(7).
[20] B Young. The behavior and design of cold-formed channel columns. PhD thesis, Sydney, Australia: University of Sydney, 1997.
[21] Mulligan GP. The influence of local buckling on the structural behavior of singly symmetric cold-formed steel columns. PhD thesis, Ithaca, New York: Cornell University, 1983.
[22] Dat DT, Pekoz TP. The strength of cold formed steel columns. Ithaca, New York: Cornell University, 1980.
[23] Thomasson P. Thin-walled C-shaped panels in axial compression. Swedish Council for Building Research, 1978.
[24] L Gao, KB Jiang, LY Bai, et al. Experimental study on stability of high strength steel long columns with box-sections[J]. Advanced Steel Construction, 2017, 13(4): 399-411.
[25] Cruise R B, Gardner L. Measurement and prediction of geometric imperfections in structural stainless steel members[J]. Structural Engineering and Mechanics, 2006, 24(1).
[26] SG Fan, RM Ding, YL Han, et al. Experimental study on bearing capacity of austenitic stainless steel lipped channel columns[J]. Advanced Steel Construction, 2020, 16(1): 65-76.
[27] L Gardner, TM Chan, JM Abela. Structural behaviour of elliptical hollow sections under combined compression and uniaxial bending[J]. Advanced Steel Construction, 2011, 7(1): 86-112.
[28] Young B, Rasmussen K. Measurement techniques in the Testing of Thin-walled Structural members[J]. Proceedings of the Society for Experimental Mechanics, 2003, 43(1).
[29] Zhao X, Tootkaboni M, Schafer B W. Development of a Laser-Based Geometric Imperfection Measurement Platform with Application to Cold-Formed Steel Construction[J]. Experimental Mechanics, 2015, 55(9).
[30] Selvaraj Sivaganesh, Madhavan Mahendrakumar. Geometric Imperfection Measurements and Validations on Cold-Formed Steel Channels Using 3D Noncontact Laser Scanner[J]. Journal of Structural Engineering, 2018, 144(3).
[31] AT Tran, L Bernspang, M Veljkovic, et al. Resistance of cold-formed high strength steel angles[J]. Advanced Steel Construction, 2019, 15(3): 242-251.
[32] Feng P, Zou Y, Hu L, et al. Use of 3D laser scanning on evaluating reduction of initial geometric imperfection of steel column with pre-stressed CFRP[J]. Engineering Structures, 2019, 198(C).
[33] N Boissonnade, H Degee, J Naumes, et al. Experimental and numerical investigations for I-girders in bending and shear stiffened by trapezoidal stiffeners[J]. Advanced Steel Construction, 2008, 4(1): 1-12.
[34] Malesa Marcin, Malowany Krzysztof, Tomczak Urszula, et al. Application of 3D digital image correlation in maintenance and process control in industry[J]. Computers in Industry, 2013, 64(9).
[35] Genovese K, Chi Y, Pan B. Stereo-camera calibration for large-scale DIC measurements with active phase targets and planar mirrors.[J]. Optics express, 2019, 27(6).
[36] Sutton M A, Ke X, Lessner S M, et al. Strain field measurements on mouse carotid arteries using microscopic three-dimensional digital image correlation.[J]. Journal of biomedical materials research. Part A, 2008, 84(1).
[37] Kepple Jendi, Herath Manudha, Pearce Garth, et al. Improved stochastic methods for modelling imperfections for buckling analysis of composite cylindrical shells[J]. Engineering Structures, 2015, 100385-398.
[38] Richard Degenhardt, Alexander Kling, Rolf Zimmermann, et al. Dealing with Imperfection Sensitivity of Composite Structures Prone to Buckling[J]. DLR, 2012.
[39] X Shao, X Dai, X He. Noise robustness and parallel computation of the inverse compositional Gauss–Newton algorithm in digital image correlation[J]. Optics and Lasers in Engineering, 2015, 71(aug.): 9-19.
[40] Yuntong Dai. External parameters optimization and high-precision pose recognition in multi-camera measurement[D]. Southeast University, 2018.
[41] Chen Xu, L Yang, N Xu, et al. Cluster approach based multi-camera digital image correlation: Methodology and its application in large area high temperature measurement[J]. Optics and Laser Technology, 2014, 57.
[42] Malowany K, Malesa M, Kowaluk T, et al. Multi-camera digital image correlation method with distributed fields of view[J]. Optics and Lasers in Engineering, 2017, 98.
[43] Genovese K, Cortese L, Rossi M, et al. A 360-deg Digital Image Correlation system for materials testing[J]. Optics and Lasers in Engineering, 2016, 82.
[44] Dong S, Yu S, Huang Z, et al. Target-based calibration method for multifields of view measurement using multiple stereo digital image correlation systems[J]. Optical Engineering, 2017, 56(12).
[45] Dong S. Applications and Key Technologies Investigation for Deformation Measurement of Large Scale Structures Using Camera Cluster[D]. Nanjing University Of Science And Technology, 2018.
[46] Arun K S, Huang T S, Blostein S D. Least-squares fitting of two 3-d point sets.[J]. IEEE transactions on pattern analysis and machine intelligence, 1987, 9(5).
[47] Heuvel F A V D, Kroon R J G A, Poole R S L. Digital close-range photogrammetry using artificial targets[J]. 1992.
[48] Besl P J, McKay H D. A method for registration of 3-D shapes[J]. IEEE Transactions on Pattern Analysis and Machine Intelligence, 1992, 14(2).
[49] ABAQUS. Abaqus Theory Manual (v6.7). 2007.